The Astrophysical Journal Supplement Series, 236:47 (14pp), 2018 June https://doi.org/10.3847/1538-4365/aabfdf

The Absolute Magnitude of the Sun in Several Filters

Christopher N. A. Willmer
Steward Observatory, University of Arizona 933 North Cherry Avenue Tucson, AZ 85721, USA; cnaw@as.arizona.edu
Received 2018 April 4; revised 2018 April 18; accepted 2018 April 19; published 2018 June 14

Abstract

This paper presents a table with estimates of the absolute magnitude of the Sun and the conversions from *vegamag* to the AB and ST systems for several wide-band filters used in ground-based and space-based observatories. These estimates use the dustless spectral energy distribution (SED) of Vega, calibrated absolutely using the SED of Sirius, to set the *vegamag* zero-points and a composite spectrum of the Sun that coadds space-based observations from the ultraviolet to the near-infrared with models of the Solar atmosphere. The uncertainty of the absolute magnitudes is estimated by comparing the synthetic colors with photometric measurements of solar analogs and is found to be ∼0.02 mag. Combined with the uncertainty of ∼2% in the calibration of the Vega SED, the errors of these absolute magnitudes are ∼3%–4%. Using these SEDs, for three of the most utilized filters in extragalactic work the estimated absolute magnitudes of the Sun are $M_B = 5.44$, $M_V = 4.81$, and $M_K = 3.27$ mag in the *vegamag* system and $M_B = 5.31$, $M_V = 4.80$, and $M_K = 5.08$ mag in AB.

Key words: astronomical databases: miscellaneous – catalogs

Supporting material: data behind figure

1. Introduction

Several astrophysical quantities, such as the masses and luminosities of stars and galaxies, are often described in terms of solar units. The luminosity density (the integral of the luminosity function) is even more specific, as it is usually expressed in terms of solar luminosities within a given photometric band (e.g., B or K). The consistent absolute calibration of flux measurements is still an essential endeavor in astrophysics, because of the expansion of wavelength coverage and the ever increasing sensitivity of instruments both from the ground and space (see Bohlin et al. 2014 for a comprehensive review). Because the first catalogs of stellar photometry used Vega as the prime calibrator (Johnson & Morgan 1953; Johnson 1955, 1966), magnitudes are commonly referred to that star. However, to overcome the effects of dust and molecular lines on stellar spectra which are difficult to model, there has been a shift to adopt either the AB system of Oke & Gunn (1983), where the calibrating spectrum is flat in f_ν, or the ST system (Bessell et al. 1998; Space Telescope Science Institute 1998), for a flat spectrum in f_λ. Both, in their turn, can be referred to observations of white dwarfs, which are calibrated through stellar models and ultimately through the use of laboratory reference standards (Bohlin et al. 2014).

Previous compilations of the Sun's absolute magnitude were published by Binney & Merrifield (1998) for the Johnson–Cousins-Glass system and Blanton et al. (2003) for the Sloan Digital Sky Survey (SDSS) filters redshifted to $z = 0.1$ in AB magnitudes. Engelke et al. (2010) calculated the *apparent* magnitude of the Sun for several filters, including the Johnson–Cousins (*UBVRI*), 2MASS (*JHK*), and *Spitzer* IRAC 8 μm and MIPS 24 μm, which can be easily converted into absolute magnitudes. The conversion constants between the *vegamag* system, where the absolute calibration is referred to Vega and the AB (Oke & Gunn 1983) and ST (Bessell et al. 1998; Space Telescope Science Institute 1998) systems for different filters, are less easy to find, and the most extensive compilation of the *vegamag* to AB measurements was published by Fukugita et al. (1995). The aim of this paper is to provide a handy reference for the absolute magnitude of the Sun in several filters used primarily by large surveys, and the additive constants (i.e., the magnitude of Vega) that transform *vegamag* into the AB and ST systems. This is done using recent determinations of the spectral energy distribution (SED) of Vega and the Sun derived from space-based observations combined with models of the atmospheres of these stars.

This paper is organized as follows. Section 2 describes the filter curves, the measurement of synthetic magnitudes, and the determination of the *vegamag* zero-points; Section 3 describes the construction of the solar spectrum; Section 4 contains a summary and conclusions.

2. Filter Curves and Synthetic Magnitudes

The filter profiles were compiled from the literature, e.g., Tonry et al. (2012), Mann & von Braun (2015), or downloaded from the databases of observatories or surveys, e.g., *JWST*, Dark Energy Survey. The filter profiles include the throughput due to the telescope, instrument optics, and detector quantum efficiency (e.g., *HST* and *JWST* filters). For *HST* filters, the latest files available in the *synphot* database[1] were used. Most of the filters used in the ground-based observations, e.g., SDSS (Gunn et al. 1998) and Pan-STARRS (Tonry et al. 2012), also include a contribution due to the Earth's atmosphere. As the *JWST* Mid Infra Red Instrument (MIRI) filter response curves of Glasse & MIRI European Consortium (2015) only contain the instrument throughput, these were multiplied by the expected *JWST* mirror reflectance as provided by the STScI NIRCam Team.

The reconstruction of the full system throughput using CCD photometry for the U, B, V bands of Johnson & Morgan (1953)

[1] http://www.stsci.edu/hst/observatory/crds/throughput.html

Table 1
Template Colors

Color (1)	Sirius[a] (2)	Bessell et al. (1998) (3)	BD+60 1753[b] (4)	IRSA[c] (5)	Rieke et al. (2008) (6)	Engelke et al. (2010) (7)
U–*B*	−0.054	−0.045	0.008	⋯	0.022	−0.029
B–*V*	−0.015	−0.01	0.023[d]	0.080[d,e]	0.001	−0.005
V–*R*	−0.013	−0.012	0.007	⋯	−0.006	0.010
R–*I*	−0.016	−0.008	0.009	⋯	−0.005	0.011
V–2MASS_K	−0.089	−0.061[f]	0.028	⋯	−0.028	−0.025
2MASS_J–2MASS_H	−0.015	−0.018[f]	0.003	−0.039	−0.004	0.008
2MASS_H–2MASS_Ks	−0.006	−0.009[f]	0.002	0.006	−0.003	−0.019
IRAC_3.6–IRAC_4.5	−0.002	⋯	−0.000	0.013	0.001	−0.003
IRAC_4.5–IRAC_5.8	−0.002	⋯	−0.000	−0.006	−0.000	−0.005
IRAC_5.8–IRAC_8.0	−0.003	⋯	−0.002	−0.010	−0.001	−0.001
WISE_1–WISE_2	−0.003	⋯	−0.000	−0.027	0.000	−0.005
WISE_2–WISE_3	−0.008	⋯	−0.005	−0.025	−0.001	−0.002
WISE_3–WISE_4	−0.006	⋯	−0.004	0.596[g]	0.000	0.010

Notes.
[a] *sirius_stis_002.fits*.
[b] NASA/IPAC Infrared Science Archive (2008) archive.
[c] *bd60d1753_stis_004.fits*.
[d] Tycho filters (Høg et al. 2000).
[e] Høg et al. (2000).
[f] Carter (1990) SAAO system.
[g] Low S/N measurement in WISE_4.

and Johnson (1955), and *R* and *I* of Cousins (1976), which were measured using photoelectric photometers, has been addressed in several works, among which are Maíz Apellániz (2006), Bessell & Murphy (2012, hereafter BM12), and Mann & von Braun (2015). In the latter work, the authors re-determine the profiles of 39 filters (*U*, *B*, *V*, *R*, and *I* among them) using spectroscopic libraries from the *HST*/STIS and IRTF/SPEX instruments, which provide coverage from the ultraviolet (UV) shortward of the atmospheric cutoff to the near-infrared. In their comparison with BM12, Mann & von Braun (2015) found agreement within 2% for most filters, a notable exception being *U*, which shows a 5% difference, which they traced to the use by BM12 of the MILES library (Falcón-Barroso et al. 2011), which has less extensive *U* coverage than the STIS spectroscopy used by Mann & von Braun (2015).

The wavelength limits of filter curves adopted in this work are set by the wavelengths where the system throughput reaches below 10^{-4} of the peak value. The filters are normalized by the maximum value and then resampled using linear interpolation because using spline interpolations can introduce spurious features in filters that do not have smooth curves (e.g., 2MASS).

The calculation of synthetic magnitudes follows BM12's Equation (A11):

$$\text{magnitude} = -2.5\log_{10}\left[\frac{\int f_{\lambda}(\lambda)R(\lambda)\lambda d\lambda}{\int R(\lambda)\lambda d\lambda}\right] - zp, \qquad (1)$$

where $f_{\lambda}(\lambda)$ is the stellar flux density in erg cm^{-2} s^{-1} Å^{-1}, $R(\lambda)$ is the product of the detector quantum efficiency × filter throughput × unitless fractional transmission of the total telescope optical train, and *zp* is the zero-point correction for a given magnitude system. The integral is calculated at each filter wavelength by determining the stellar flux value using linear interpolation.

The AB system is defined such that the zero-point flux density for every filter is 3631 Jy, corresponding to a $zp = +48.6$ For the ST system the $zp = +21.1$ and is defined such that the magnitude of Vega in the (Johnson) *V* band is +0.03 (Bessell et al. 1998). In both cases these zero-points assume the standard calibration spectrum is flat either in frequency (AB) or wavelength (ST) (Space Telescope Science Institute 1998).

In the case of the Johnson (1966) *UBVRI* or *vegamag* (Space Telescope Science Institute 1998) system, the zero-point is defined from the colors of several A stars, and because of this, Vega has a small magnitude offset in all bands that must be accounted for when using its spectrum as a flux standard (Rieke et al. 2008). However, the finding that Vega's spectrum shows the presence of a debris disk (Aumann et al. 1984; Rieke et al. 2008; Su et al. 2013; Bohlin 2014), and that in addition is a rapid rotator (Peterson et al. 2006), limits the ability of theoretical models of matching its SED, and has prompted the search of other AV stars to serve as spectral flux standards, e.g., Cohen et al. (1992), Bessell et al. (1998), Engelke et al. (2010), Bohlin (2014).

The use of Sirius as a flux standard for the infrared was initially proposed by Cohen et al. (1992), and adopted by Bessell et al. (1998) and Engelke et al. (2010). A detailed analysis of the SED of Sirius was done by Bohlin (2014) who created a template combining *IUE* and *HST*/STIS spectra for wavelengths between ∼0.15 and 1.0 μm with a Kurucz model of Sirius to 300 μm. Bohlin (2014) found the STIS measurements to agree to better than 1% with the Kurucz model and that this model also shows good agreement (∼2%) with infrared photometry obtained by the *Midcourse Space Experiment* (*MSX*) satellite. Based on these results, Bohlin (2014) concluded that Sirius can be used as a standard

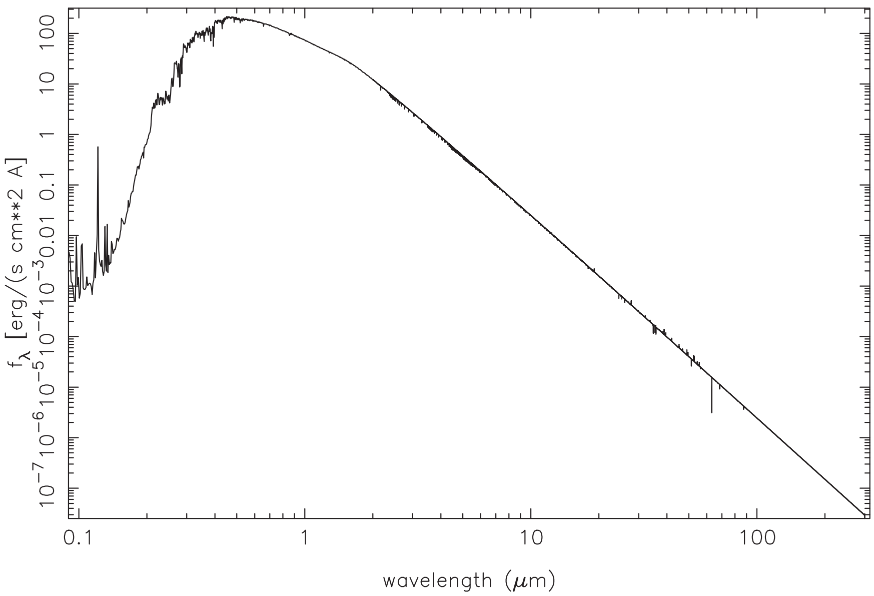

Figure 1. Composite spectrum of the Sun, combining the observed spectrum of Haberreiter et al. (2017) to 2.0 μm, the Fontenla et al. (2011) model between 2.0 and 100 μm and the Kurucz model *Sun_mod_001.fits* from 100 to 300 μm. The data used to create this figure are available.

calibrator for the infrared and its composite spectrum is available in the *CALSPEC* database (*sirius_stis_002.fits*). After adopting Sirius as the flux standard, Bohlin (2014) renormalized the Vega composite dust-free template spectrum that combines *IUE* and STIS observations of Vega with two Kurucz models for Vega with $T = 9550$ K (for the extreme UV) and $T = 9400$ K (for the visible-far-IR) (Bohlin 2014), which is file *alpha_lyr_stis_008.fits* in the *CALSPEC* database.

Other AV templates have been defined using models and observations. Rieke et al. (2008) constructed a dustless A0V template using the Kurucz (2005) model of Vega and normalized the spectrum in the infrared after correcting for the contribution of the debris disk. By means of a detailed comparison with the photometry of A dwarfs and solar analogs Rieke et al. (2008) showed that this A0V template, as well as the solar SED they calculated in the same paper, give consistent calibrations for the infrared. An AV template combining ground-based observations of 109 Vir with the average NICMOS observations for eight A type stars, *ISO* observations of Sirius (from 2.4 to 9.4 μm), and beyond 9.4 μm, a Kurucz model spectrum for Sirius, was compiled by Engelke et al. (2010), who found that the calibration uncertainties are $\lesssim$2%. The final template considered here is the A1V star BD+60 1753, which is one of the *IRAC* calibrators (Reach et al. 2005) that has a *CALSPEC* spectrum *bd60d1753_stis_004.fits*, which combines *HST*/STIS observations from 1140 to 10120 Å with BOSZ models beyond 10120 Å (Bohlin et al. 2017).

A comparison between colors measured using the Bohlin (2014) *alpha_lyr_stis_008.fits* spectrum of Vega as a standard (which will be zero by definition) with those of the AV templates discussed above is shown Table 1. Column (1) is the photometric color, column (2) is the synthetic color measured using the Sirius spectrum of Bohlin (2014), and column (3) is photometric measurement of Sirius in Bessell et al. (1998). Column (4) shows the synthetic photometry colors for BD+60 1753, while column (5) shows the measurements for this star available in Høg et al. (2000) and the NASA/IPAC Infrared Science Archive (2008) archive. Columns (6) and (7) show the synthetic colors measured for the Rieke et al. (2008) and Engelke et al. (2010) templates, respectively. The average differences between the synthetic and observed colors of Sirius and BD+60 1753 are -0.006 ± 0.010 and and 0.007 ± 0.028, respectively. The mean difference between the synthetic colors measured for the four templates and the Vega SED are $\lesssim$0.018 mag, with a dispersion of the same order of magnitude ($\lesssim$0.024 mag). These results suggest that the calibration uncertainty introduced by using the *CALSPEC* spectrum of Vega is ~2%.

In this work the *vegamag* magnitudes are calculated using the Vega SED of Bohlin (2014) (*alpha_lyr_stis_008.fits* in the STScI *CALSPEC* database), assuming a Vega magnitude of $V = 0.03$ (BM12).

3. The Solar Spectrum

The solar SED used here also combines observations with model spectra. The observed spectrum is a composite calculated by Haberreiter et al. (2017) using data from over 20 space-based instruments for an arbitrary date (2008 December 19, JDN = 2454820) during the solar minimum. Spectra for other dates around the solar minimum show no significant change relative to the spectrum adopted here. Haberreiter et al. (2017) used a probabilistic approach to combine observations at each timestep, weighting the spectra by their uncertainties and accounting for fluctuations over time between different instruments at the same wavelength. The absolute calibration is set using the *ATLAS* 3 composite spectrum of Thuillier et al. (2004), and constraining the Total Solar Irradiance (TSI) to the value measured for each day by Dudok de Wit et al. (2017). The observed composite ends at ~2.0 μm, and to extend the SED into the infrared; the model spectra of Fontenla et al. (2011)

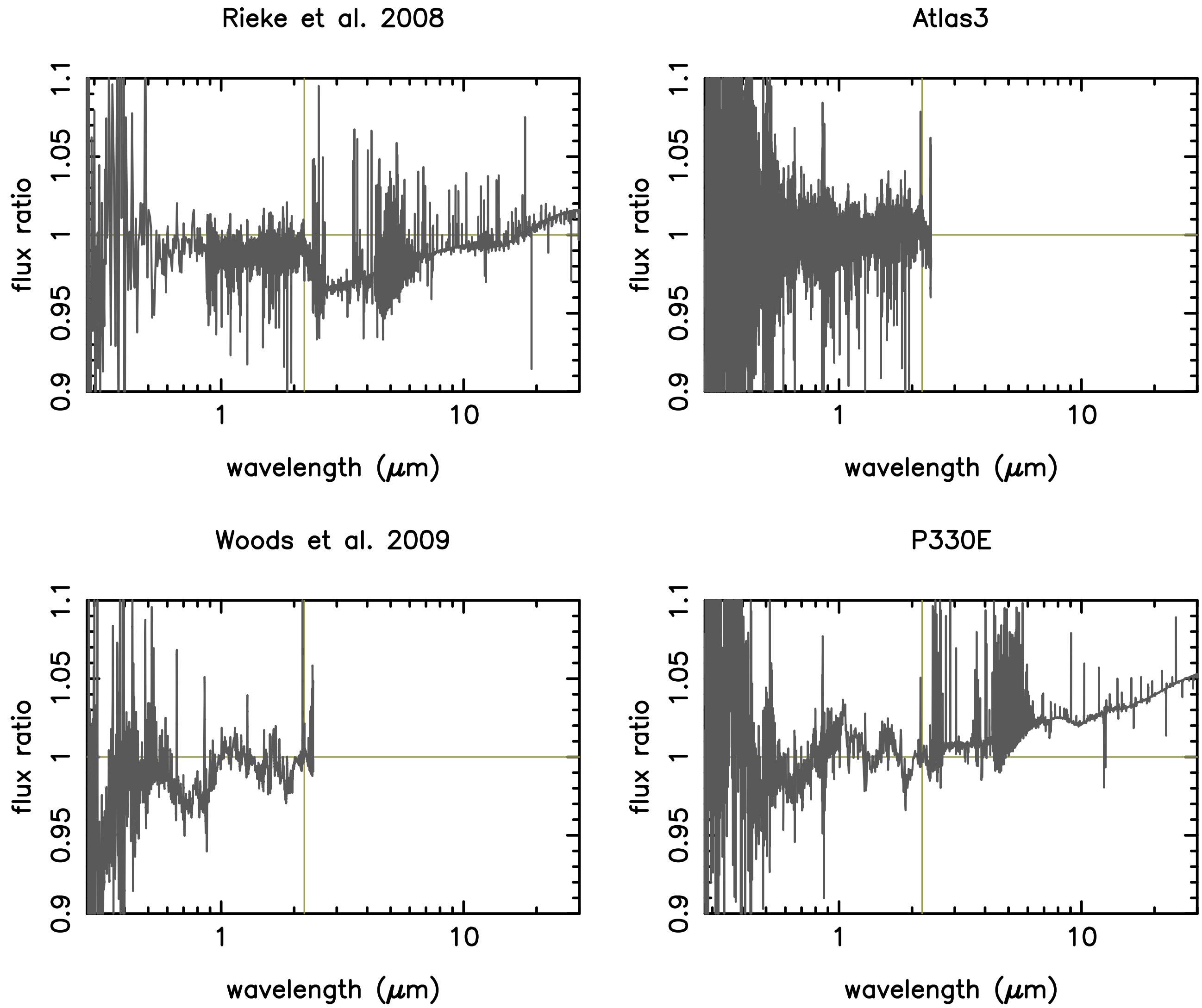

Figure 2. Ratio between published SEDs of the Sun and the composite used here. The panels show the ratio for the Rieke et al. (2008), ATLAS-3 (Thuillier et al. 2004), Woods et al. (2009) and the solar analog P330E from the Space Telescope Science Institute (2017a) database, normalized to have the same flux as the composite spectrum at 2.2 μm. The vertical line is located at $\lambda = 2.2$ μm. The spikes seen in these ratios are caused by small mismatches in the wavelengths and resolutions of the spectra. Differences of the order of ~5% can be seen in the ratios between spectra. The Rieke et al. (2008) spectrum between 2.2 and 20 μm where the Engelke (1992) approximation is used, is systematically fainter than the Fontenla et al. (2011) models, while shortward of 2.2 μm the agreement with the composite adopted here is very good. The spectrum of P330E is systematically brighter than the composite used here for wavelengths longer than ~2 μm.

and Kurucz (2011) are used. The Fontenla et al. (2011) model uses the Solar Irradiance Physical Modeling system to produce solar irradiance spectra from 0.012 to 100 μm through a combination of non-LTE models with semi-empirical physical models derived from observed spectra to produce the solar SED. The Fontenla et al. (2011) spectrum was scaled by the bi-weight average (Beers et al. 1990) ratio between the Haberreiter et al. (2017) composite and the model for wavelengths between 1.8 μm and 2.0 μm (1.0299 ± 0.0074). Beyond 100 μm, the special Kurucz model at $R = 5000$ calculated for the *CALSPEC* database (*Sun_mod_001.fits*, Kurucz 2011) is used, and to eliminate any discontinuities in the transition between source spectra, the bi-weight ratio between the re-normalized Fontenla et al. (2011) and Kurucz models, calculated between 90 and 100.0 μm (0.9940 ± 0.0073), was used to scale the latter. Figure 1 shows the composite spectrum.

Figure 2 shows the ratios between this composite spectrum with other determinations in the literature—Rieke et al. (2008), Thuillier et al. (2004), Woods et al. (2009). Also shown is a comparison with the solar analog P330E after scaling its spectrum to have the same flux density as the composite at 2.2 μm (8.58593 erg cm^{-2} s^{-1} Å^{-1}). The ratios being plotted are calculated at each tabulated wavelength of the source spectrum and estimating the composite's flux using linear interpolation. The SED ratios are very close to 1 (0.998, 1.005, 0.993, and 1.017 for Rieke et al. (2008), Thuillier et al. (2004), Woods et al. (2009) and P330E, respectively) and dispersions of 0.037 or better, in all cases using the bi-weight estimator. The rms fluctuations range from 0.02 for the Rieke et al. (2008) solar spectrum, to 0.22 in the case of P330E.

A comparison between colors estimated using the solar composite spectrum with measurements by Ramírez et al. (2012)

Table 2
Colors of the Solar Composite Compared to Solar Analogs

Color	Composite	Solar Analogs	Difference	Rieke et al. (2008) SED	Difference
U–*B*	0.164	0.166[a]	−0.002	0.138	0.026
B–*V*	0.629	0.653[a]	−0.024	0.629	0.000
V–*R*	0.387	0.352[a]	0.035	0.388	−0.001
V–*I*	0.712	0.702[a]	0.010	0.717	−0.005
V–2MASS_J	1.145	1.198[b]	−0.053	1.143	0.002
V–2MASS_H	1.494	1.484[b]	0.010	1.492	0.002
V–2MASS_Ks	1.542	1.560[b]	−0.018	1.545	−0.003
V–WISE_1	1.553	1.608[b]	−0.055	1.530	0.023
V–WISE_2	1.530	1.563[b]	−0.033	1.515	0.015
V–WISE_3	1.549	1.552[b]	−0.003	1.551	−0.002
V–WISE_4	1.539	1.604[b]	−0.065	1.559	−0.020

Notes.
[a] Ramírez et al. (2012).
[b] Casagrande et al. (2012).

and Casagrande et al. (2012) of solar analogs is presented in Table 2. The average difference in colors for (composite—solar analogs) is -0.018 ± 0.030 mag, suggesting that the composite spectrum shows consistent measurements both in the UV–visible and the infrared. Table 2 also compares the colors of the new composite with measurements using the Rieke et al. (2008) solar model, which combines the Thuillier et al. (2003) SED with the Engelke (1992) approximation for the near to mid-infrared. The (composite—Rieke et al. 2008) differences are -0.003 ± 0.013 mag, though these measurements may not be completely independent as Haberreiter et al. (2017) use the Thuillier et al. (2004) spectrum to set the absolute calibration of the solar spectrum.

The estimated errors in the solar magnitudes change as a function of wavelength due to the uncertainty on the absolute calibration using the Vega and Solar SED $\sim$ 2%–3% (Rieke et al. 2008; Bohlin 2014). When these are added in quadrature it results in uncertainties $\sim$3% over the range covered by solar analogs. These can become larger ($\sim$5%) as one transitions toward the mid-infrared due to the difficulty in calibrating the space-based instruments in this wavelength range, e.g., Fontenla et al. (2011).

To derive the Sun's absolute magnitudes, the IAU 2012 definitions of the astronomical unit (au) (Prša et al. 2016) and parsec were used, giving a distance modulus for the Sun of -31.5721 mag. To rationalize the use of solar constants, the IAU in 2015 adopted a nominal value for the Sun's luminosity $L_\odot = 3.828 \times 10^8$ W (Prša et al. 2016), which corresponds to an average TSI of 1361 W m^{-2} at 1 au and an absolute bolometric magnitude of $M_{\rm Bol} = 4.74$.

The columns of Table 3 contain the following: (1) the filter; (2)–(4) the absolute magnitude of the Sun in the *vegamag*, AB, and ST systems, respectively; (5)–(7) the apparent magnitude in *vegamag*, AB, and ST; (8) and (9) tabulated offsets between the *vegamag* and AB and *vegamag* and ST systems; (10) the pivot wavelength; and (11) the source of the throughput curves, identified in the table notes.

4. Summary

This work uses the dust-free composite spectrum of Vega with the absolute calibration set by Sirius, both from Bohlin (2014), to calculate a table with the absolute magnitude of the Sun and the conversion between the *vegamag* and the AB and ST systems for several filters used in ground-based and space-based observatories. The solar SED used in this paper is a composite combining space-based spectra of the Sun from the ultraviolet to the near-infrared (Haberreiter et al. 2017), with models of the solar atmosphere out to 300 μm (Fontenla et al. 2011; Kurucz 2011). For the set of Johnson (U, B, V) and Cousins (R and I) filters, which were originally characterized using photoelectric photometry, filter curves reconstructed using Monte Carlo methods by Mann & von Braun (2015) are used. To verify the consistency of the synthetic spectra measured using the composite spectra of Vega and the Sun, the colors measured for these SEDs are compared with photometric measurements of AV stellar templates and solar analogs, respectively. A comparison between colors calculated for the Vega SED and AV stars shows absolute offsets $<$0.01 mag and a dispersion $<$0.03 mag, consistent with the estimated uncertainty at the 2% level for the Vega SED by Bohlin (2014). The comparison between colors measured with the solar composite and the solar analogs of Ramírez et al. (2012) and Casagrande et al. (2012) shows an offset of $\sim -0.02 \pm 0.03$ mag. Assuming the errors are equally distributed, this translates to an average uncertainty of $\sim$2% for the solar SED. Adding in quadrature the uncertainty in the calibration of both spectra translates to errors $\sim$3%–4% for the solar absolute magnitudes.

I thank George Rieke for suggestions and discussions. I also thank the anonymous referee and the editor Dr. Shadia Habbal, whose suggestions helped improve the presentation. Funding from the *JWST*/NIRCam contract NAS5-02015 to the University of Arizona, the use of the NASA/SAO ADS, the NASA/IPAC Infrared Science Archive, Simbad (at Strasbourg and Harvard), and the Mikulski Archive for Space Telescopes are gratefully acknowledged. This work uses data from the SOLID Project http://projects.pmodwrc.ch/solid/, which is funded by the European Community's Seventh Framework Programme (FP7 2012) under grant agreement no 313188.

Facilities: IRSA, MAST, *JWST*-Docs, *GALEX*, ADS, CDS.

Table 3
Magnitudes of the Sun

Filter (1)	Abs (Vega) (2)	Abs (AB) (3)	Abs (ST) (4)	App (Vega) (5)	App (AB) (6)	App (ST) (7)	Vega (AB) (8)	Vega (ST) (9)	$\lambda_{\rm pivot}$ (μm) (10)	Source (11)
Johnson_U	5.61	6.33	5.42	−25.97	−25.25	−26.15	0.721	−0.183	0.3611	1
Johnson_B	5.44	5.31	4.84	−26.13	−26.26	−26.74	−0.128	−0.605	0.4396	1
Johnson_V	4.81	4.80	4.81	−26.76	−26.77	−26.76	−0.013	0.001	0.5511	1
Cousins_R	4.43	4.60	5.00	−27.15	−26.97	−26.57	0.178	0.578	0.6582	1
Cousins_I	4.10	4.51	5.35	−27.47	−27.06	−26.22	0.414	1.247	0.8034	1
Tycho_Bt	5.58	5.48	4.91	−25.99	−26.09	−26.66	−0.097	−0.667	0.4212	1
Tycho_Vt	4.88	4.85	4.79	−26.69	−26.72	−26.78	−0.035	−0.091	0.5335	1
Hipparcos_Hp	4.87	4.87	4.88	−26.70	−26.70	−26.69	−0.002	0.011	0.5508	1
2MASS_J	3.67	4.54	6.31	−27.90	−27.03	−25.26	0.870	2.644	1.2393	2
2MASS_H	3.32	4.66	7.06	−28.25	−26.91	−24.51	1.344	3.739	1.6495	2
2MASS_Ks	3.27	5.08	8.07	−28.30	−26.49	−23.50	1.814	4.798	2.1638	2
SDSS_u	5.49	6.39	5.45	−26.08	−25.18	−26.12	0.900	−0.037	0.3556	3
SDSS_g	5.23	5.11	4.78	−26.34	−26.47	−26.80	−0.125	−0.456	0.4702	3
SDSS_r	4.53	4.65	4.91	−27.04	−26.93	−26.66	0.119	0.380	0.6176	3
SDSS_i	4.19	4.53	5.21	−27.38	−27.05	−26.37	0.332	1.012	0.7490	3
SDSS_z	4.01	4.50	5.57	−27.56	−27.07	−26.00	0.494	1.560	0.8947	3
DES_u	5.83	6.14	5.38	−25.74	−25.44	−26.20	0.307	−0.452	0.3859	4
DES_g	5.17	5.05	4.78	−26.41	−26.52	−26.80	−0.114	−0.391	0.4820	4
DES_r	4.45	4.61	4.96	−27.12	−26.96	−26.61	0.159	0.505	0.6423	4
DES_i	4.14	4.52	5.29	−27.43	−27.05	−26.28	0.382	1.152	0.7807	4
DES_z	4.01	4.50	5.62	−27.56	−27.07	−25.95	0.493	1.610	0.9158	4
DES_Y	3.96	4.50	5.78	−27.61	−27.07	−25.79	0.540	1.819	0.9866	4
PS1_g	5.14	5.03	4.77	−26.43	−26.54	−26.80	−0.112	−0.376	0.4849	5
PS1_r	4.53	4.64	4.92	−27.05	−26.93	−26.66	0.120	0.390	0.6201	5
PS1_i	4.18	4.52	5.22	−27.39	−27.05	−26.35	0.339	1.033	0.7535	5
PS1_z	4.02	4.51	5.50	−27.55	−27.07	−26.07	0.483	1.482	0.8674	5
PS1_Y	3.99	4.50	5.73	−27.59	−27.07	−25.85	0.515	1.741	0.9628	5
cfhtls_u	5.70	6.04	5.25	−25.87	−25.53	−26.33	0.336	−0.455	0.3803	6
cfhtls_g	5.15	5.03	4.77	−26.42	−26.54	−26.80	−0.116	−0.382	0.4844	6
cfhtls_r	4.50	4.64	4.92	−27.07	−26.94	−26.65	0.131	0.417	0.6248	6
cfhtls_i	4.16	4.52	5.26	−27.41	−27.05	−26.32	0.362	1.096	0.7678	6
cfhtls_z	4.02	4.51	5.55	−27.56	−27.07	−26.02	0.490	1.535	0.8859	6
CFHT_12kx8k_B	5.43	5.28	4.80	−26.14	−26.30	−26.77	−0.157	−0.632	0.4399	7
CFHT_12kx8k_R	4.39	4.59	5.00	−27.18	−26.98	−26.57	0.196	0.605	0.6610	7
CFHT_12kx8k_I	4.10	4.51	5.38	−27.47	−27.06	−26.19	0.415	1.282	0.8159	7
UKIRT_z	4.02	4.51	5.54	−27.56	−27.07	−26.03	0.489	1.526	0.8826	8
UKIRT_Y	3.92	4.51	5.88	−27.66	−27.07	−25.69	0.591	1.966	1.0315	8
UKIRT_J	3.65	4.54	6.33	−27.92	−27.03	−25.24	0.891	2.684	1.2502	8
UKIRT_H	3.33	4.66	7.03	−28.25	−26.92	−24.54	1.329	3.705	1.6360	8
UKIRT_K	3.27	5.12	8.14	−28.30	−26.45	−23.43	1.848	4.874	2.2060	8
LSST_u	5.65	6.27	5.40	−25.93	−25.30	−26.17	0.627	−0.244	0.3665	9
LSST_g	5.17	5.06	4.77	−26.40	−26.52	−26.80	−0.116	−0.399	0.4808	9
LSST_r	4.52	4.64	4.92	−27.05	−26.93	−26.66	0.121	0.395	0.6210	9
LSST_i	4.18	4.52	5.22	−27.39	−27.05	−26.35	0.340	1.034	0.7537	9
LSST_z	4.02	4.51	5.51	−27.55	−27.07	−26.06	0.484	1.486	0.8686	9
LSST_y	3.98	4.50	5.74	−27.59	−27.07	−25.83	0.520	1.763	0.9705	9
Bessell_Murphy_U	5.57	6.34	5.43	−26.00	−25.23	−26.14	0.768	−0.144	0.3597	10
Bessell_Murphy_B	5.46	5.33	4.84	−26.11	−26.24	−26.73	−0.134	−0.620	0.4378	10
Bessell_Murphy_V	4.82	4.81	4.81	−26.75	−26.77	−26.76	−0.017	−0.012	0.5489	10
Bessell_Murphy_R	4.44	4.61	4.99	−27.13	−26.96	−26.58	0.168	0.548	0.6524	10
Bessell_Murphy_I	4.11	4.52	5.33	−27.46	−27.06	−26.24	0.408	1.227	0.7984	10
Bessell_Murphy_Bt	5.60	5.51	4.93	−25.98	−26.06	−26.65	−0.088	−0.669	0.4190	10
Bessell_Murphy_Vt	4.89	4.86	4.79	−26.68	−26.71	−26.79	−0.038	−0.108	0.5300	10
Bessell_Murphy_Hp	4.93	4.92	4.86	−26.64	−26.66	−26.71	−0.018	−0.068	0.5349	10
Bessell_88_J	3.67	4.54	6.30	−27.90	−27.03	−25.27	0.866	2.632	1.2347	11
Bessell_88_H	3.32	4.66	7.05	−28.25	−26.91	−24.52	1.337	3.726	1.6450	11
Bessell_88_K	3.27	5.09	8.07	−28.30	−26.49	−23.50	1.815	4.802	2.1663	11
Bessell_88_L	3.26	5.98	10.00	−28.31	−25.59	−21.58	2.721	6.737	3.4797	11
Bessell_88_Lprime	3.26	6.17	10.39	−28.31	−25.40	−21.18	2.914	7.135	3.8247	11
Bessell_88_M	3.29	6.64	11.33	−28.28	−24.93	−20.25	3.349	8.034	4.7347	11
GALEX_FUV	15.22	17.30	14.54	−16.36	−14.27	−17.03	2.085	−0.676	0.1535	12
GALEX_NUV	8.53	10.16	8.28	−23.04	−21.41	−23.30	1.629	−0.253	0.2301	12

Table 3
(Continued)

Filter (1)	Abs (Vega) (2)	Abs (AB) (3)	Abs (ST) (4)	App (Vega) (5)	App (AB) (6)	App (ST) (7)	Vega (AB) (8)	Vega (ST) (9)	λ_{pivot} (μm) (10)	Source (11)
WISE_1	3.26	5.91	9.87	−28.31	−25.66	−21.70	2.655	6.614	3.3897	13
WISE_2	3.28	6.57	11.22	−28.29	−25.00	−20.36	3.291	7.932	4.6406	13
WISE_3	3.26	8.48	15.28	−28.31	−23.09	−16.29	5.215	12.019	12.5705	13
WISE_4	3.27	9.88	17.93	−28.30	−21.70	−13.65	6.602	14.652	22.3142	13
IRAS12	3.26	8.30	14.89	−28.31	−23.27	−16.69	5.037	11.621	11.3562	13
IRAS25	3.27	9.92	18.09	−28.30	−21.65	−13.48	6.646	14.819	23.6079	13
IRAS60	3.28	11.90	22.12	−28.29	−19.67	−9.46	8.621	18.833	60.3699	13
IRAS100	3.29	13.14	24.47	−28.28	−18.43	−7.10	9.854	21.186	101.1267	13
IRAC_3.6	3.26	6.02	10.08	−28.31	−25.56	−21.50	2.758	6.817	3.5508	13
IRAC_4.5	3.28	6.51	11.08	−28.29	−25.06	−20.49	3.232	7.804	4.4960	13
IRAC_5.8	3.28	7.00	12.09	−28.30	−24.58	−19.48	3.720	8.816	5.7245	13
IRAC_8.0	3.26	7.62	13.41	−28.31	−23.95	−18.16	4.360	10.152	7.8842	13
IRS_16	3.27	9.11	16.42	−28.31	−22.47	−15.15	5.839	13.157	15.9222	13
IRS_22	3.27	9.86	17.92	−28.30	−21.72	−13.65	6.584	14.650	22.4704	14
MIPS_24	3.27	10.01	18.19	−28.30	−21.57	−13.38	6.731	14.918	23.7592	14
MIPS_70	3.29	12.40	23.00	−28.28	−19.17	−8.58	9.114	19.708	71.9861	14
MIPS_160	3.29	14.15	26.42	−28.28	−17.43	−5.15	10.857	23.137	156.4274	14
ACS_F330W	5.34	6.43	5.47	−26.24	−25.14	−26.10	1.097	0.139	0.3521	14
ACS_F410W	5.70	5.67	5.02	−25.87	−25.90	−26.55	−0.033	−0.680	0.4064	14
ACS_F435W	5.48	5.35	4.84	−26.09	−26.22	−26.73	−0.129	−0.639	0.4328	14
ACS_F475W	5.21	5.09	4.78	−26.36	−26.49	−26.80	−0.122	−0.432	0.4747	14
ACS_F555W	4.87	4.84	4.79	−26.71	−26.74	−26.78	−0.030	−0.076	0.5361	14
ACS_F606W	4.66	4.72	4.89	−26.92	−26.85	−26.68	0.063	0.233	0.5922	14
ACS_F625W	4.49	4.63	4.94	−27.08	−26.94	−26.64	0.140	0.448	0.6312	14
ACS_F775W	4.16	4.52	5.26	−27.42	−27.05	−26.31	0.364	1.103	0.7694	14
ACS_F814W	4.12	4.52	5.36	−27.46	−27.06	−26.22	0.400	1.239	0.8059	14
ACS_F850LP	4.01	4.50	5.59	−27.56	−27.07	−25.98	0.494	1.577	0.9016	14
WFC3_F218W	9.09	10.74	8.79	−22.48	−20.83	−22.78	1.654	−0.298	0.2229	14
WFC3_F225W	8.51	10.13	8.32	−23.06	−21.44	−23.25	1.625	−0.191	0.2372	14
WFC3_F336W	5.49	6.64	5.58	−26.09	−24.93	−25.99	1.158	0.094	0.3355	14
WFC3_F390W	5.66	5.85	5.12	−25.91	−25.73	−26.45	0.187	−0.536	0.3924	14
WFC3_F438W	5.50	5.32	4.81	−26.07	−26.25	−26.76	−0.178	−0.690	0.4326	14
WFC3_F475W	5.19	5.07	4.77	−26.38	−26.50	−26.80	−0.122	−0.419	0.4774	14
WFC3_F555W	4.91	4.86	4.79	−26.67	−26.72	−26.78	−0.048	−0.116	0.5308	14
WFC3_F606W	4.67	4.73	4.88	−26.91	−26.85	−26.69	0.059	0.217	0.5887	14
WFC3_F625W	4.52	4.64	4.92	−27.06	−26.93	−26.65	0.124	0.409	0.6241	14
WFC3_F775W	4.16	4.52	5.25	−27.41	−27.05	−26.33	0.357	1.083	0.7648	14
WFC3_F814W	4.12	4.52	5.35	−27.45	−27.06	−26.22	0.395	1.226	0.8030	14
WFC3_F098m	3.96	4.50	5.78	−27.61	−27.07	−25.79	0.538	1.816	0.9864	14
WFC3_F105W	3.89	4.51	5.94	−27.68	−27.06	−25.63	0.622	2.046	1.0551	14
WFC3_F125W	3.66	4.54	6.33	−27.91	−27.03	−25.24	0.877	2.667	1.2486	14
WFC3_F140W	3.51	4.56	6.59	−28.06	−27.01	−24.98	1.052	3.079	1.3922	14
WFC3_F160W	3.37	4.60	6.84	−28.20	−26.97	−24.73	1.228	3.469	1.5370	14
WFPC2_F218W	9.17	10.83	8.86	−22.40	−20.74	−22.72	1.657	−0.316	0.2207	15
WFPC2_F300W	6.10	7.40	6.09	−25.48	−24.17	−25.48	1.307	−0.005	0.2992	15
WFPC2_F450W	5.31	5.20	4.80	−26.26	−26.37	−26.77	−0.110	−0.509	0.4556	15
WFPC2_F555W	4.84	4.82	4.81	−26.73	−26.75	−26.77	−0.025	−0.038	0.5442	15
WFPC2_F606W	4.62	4.70	4.90	−26.95	−26.87	−26.67	0.077	0.276	0.6001	15
WFPC2_F702W	4.33	4.57	5.08	−27.24	−27.00	−26.49	0.240	0.748	0.6919	15
WFPC2_F814W	4.12	4.52	5.34	−27.45	−27.05	−26.23	0.392	1.216	0.8002	15
NIC2_F110W	3.82	4.52	6.08	−27.75	−27.05	−25.49	0.704	2.265	1.1235	15
NIC2_F160W	3.35	4.64	6.97	−28.22	−26.93	−24.60	1.286	3.618	1.6030	15
NIC3_F110W	3.82	4.52	6.08	−27.75	−27.05	−25.50	0.701	2.255	1.1200	15
NIC3_F160W	3.35	4.64	6.97	−28.22	−26.93	−24.60	1.287	3.621	1.6042	15
NIRCAM_F070W	4.29	4.56	5.10	−27.28	−27.02	−26.47	0.264	0.811	0.7046	15
NIRCAM_F090W	4.02	4.50	5.59	−27.56	−27.07	−25.98	0.488	1.573	0.9025	15
NIRCAM_F115W	3.77	4.53	6.15	−27.80	−27.05	−25.43	0.753	2.373	1.1543	15
NIRCAM_F140M	3.48	4.56	6.60	−28.09	−27.02	−24.97	1.079	3.126	1.4053	15
NIRCAM_F150W	3.41	4.59	6.78	−28.16	−26.98	−24.79	1.182	3.371	1.5007	15
NIRCAM_F150W2	3.50	4.70	7.11	−28.07	−26.87	−24.46	1.203	3.610	1.6588	15
NIRCAM_F162M	3.32	4.65	7.01	−28.25	−26.93	−24.56	1.328	3.693	1.6272	15
NIRCAM_F164N	3.29	4.66	7.05	−28.28	−26.91	−24.53	1.368	3.756	1.6445	15

Table 3
(Continued)

Filter (1)	Abs (Vega) (2)	Abs (AB) (3)	Abs (ST) (4)	App (Vega) (5)	App (AB) (6)	App (ST) (7)	Vega (AB) (8)	Vega (ST) (9)	λ_{pivot} (μm) (10)	Source (11)
NIRCAM_F182M	3.28	4.81	7.45	−28.29	−26.76	−24.12	1.534	4.172	1.8452	15
NIRCAM_F187N	3.25	4.85	7.52	−28.33	−26.72	−24.05	1.600	4.272	1.8739	15
NIRCAM_F200W	3.28	4.93	7.73	−28.30	−26.64	−23.84	1.652	4.453	1.9886	15
NIRCAM_F200W	3.28	4.93	7.73	−28.30	−26.64	−23.84	1.652	4.453	1.9886	15
NIRCAM_F210M	3.27	5.03	7.94	−28.30	−26.54	−23.63	1.757	4.671	2.0955	15
NIRCAM_F250M	3.27	5.37	8.67	−28.30	−26.21	−22.91	2.093	5.393	2.5032	15
NIRCAM_F277W	3.26	5.53	9.04	−28.31	−26.04	−22.53	2.265	5.779	2.7618	15
NIRCAM_F300M	3.26	5.69	9.37	−28.31	−25.88	−22.20	2.429	6.115	2.9892	15
NIRCAM_F322W2	3.26	5.77	9.63	−28.31	−25.80	−21.95	2.509	6.365	3.2320	15
NIRCAM_F323N	3.26	5.84	9.70	−28.31	−25.73	−21.87	2.583	6.441	3.2369	15
NIRCAM_F335M	3.26	5.92	9.86	−28.31	−25.66	−21.71	2.658	6.599	3.3621	15
NIRCAM_F356W	3.26	6.02	10.09	−28.31	−25.55	−21.48	2.763	6.833	3.5684	15
NIRCAM_F405N	3.24	6.30	10.65	−28.33	−25.27	−20.93	3.058	7.404	4.0517	15
NIRCAM_F410M	3.26	6.31	10.67	−28.32	−25.27	−20.90	3.049	7.411	4.0822	15
NIRCAM_F430M	3.27	6.41	10.88	−28.31	−25.16	−20.69	3.147	7.613	4.2813	15
NIRCAM_F444W	3.27	6.46	10.99	−28.30	−25.11	−20.59	3.185	7.712	4.4040	15
NIRCAM_F460M	3.29	6.60	11.23	−28.28	−24.97	−20.34	3.308	7.943	4.6285	15
NIRCAM_F466N	3.26	6.62	11.26	−28.31	−24.96	−20.31	3.352	8.000	4.6544	15
NIRCAM_F470N	3.29	6.63	11.30	−28.28	−24.94	−20.27	3.341	8.013	4.7078	15
NIRCAM_F480M	3.29	6.67	11.39	−28.28	−24.90	−20.18	3.383	8.104	4.8167	15
MIRI_F560W	3.28	6.97	12.03	−28.29	−24.60	−19.54	3.693	8.756	5.6362	16
MIRI_F770W	3.26	7.58	13.30	−28.31	−24.00	−18.27	4.314	10.039	7.6428	16
MIRI_F1000W	3.26	8.15	14.45	−28.31	−23.42	−17.13	4.883	11.181	9.9544	16
MIRI_F1130W	3.26	8.43	15.00	−28.31	−23.14	−16.57	5.166	11.741	11.3087	16
MIRI_F1500W	3.27	9.03	16.23	−28.31	−22.54	−15.35	5.763	12.961	15.0651	16
MIRI_F1800W	3.27	9.42	17.00	−28.30	−22.15	−14.57	6.149	13.732	17.9865	16
MIRI_F2100W	3.27	9.72	17.62	−28.30	−21.85	−13.95	6.453	14.351	20.7950	16
MIRI_F2550W	3.28	10.16	18.49	−28.30	−21.41	−13.08	6.887	15.216	25.3639	16
NIRISS_F090W	4.02	4.50	5.59	−27.56	−27.07	−25.98	0.488	1.575	0.9031	17
NIRISS_F115W	3.78	4.53	6.14	−27.79	−27.05	−25.43	0.747	2.358	1.1499	17
NIRISS_F140M	3.48	4.56	6.60	−28.09	−27.02	−24.97	1.078	3.123	1.4044	17
NIRISS_F150W	3.41	4.59	6.77	−28.16	−26.98	−24.81	1.173	3.352	1.4936	17
NIRISS_F158M	3.35	4.62	6.93	−28.23	−26.95	−24.64	1.277	3.582	1.5825	17
NIRISS_F200W	3.28	4.93	7.74	−28.30	−26.64	−23.83	1.656	4.461	1.9930	17
NIRISS_F277W	3.27	5.53	9.04	−28.30	−26.05	−22.53	2.258	5.774	2.7641	17
NIRISS_F356W	3.26	6.03	10.11	−28.31	−25.54	−21.46	2.769	6.854	3.5926	17
NIRISS_F380M	3.26	6.17	10.39	−28.31	−25.40	−21.18	2.908	7.128	3.8229	17
NIRISS_F430M	3.27	6.40	10.87	−28.30	−25.17	−20.70	3.130	7.595	4.2792	17
NIRISS_F444W	3.27	6.47	11.00	−28.30	−25.11	−20.57	3.191	7.729	4.4270	17
NIRISS_F480M	3.29	6.66	11.38	−28.28	−24.91	−20.19	3.366	8.086	4.8113	17
OMEGACAM_u	5.46	6.34	5.43	−26.11	−25.23	−26.15	0.881	−0.035	0.3590	18
OMEGACAM_g	5.21	5.09	4.77	−26.36	−26.48	−26.80	−0.126	−0.442	0.4735	18
OMEGACAM_r	4.50	4.63	4.93	−27.07	−26.94	−26.64	0.133	0.429	0.6276	18
OMEGACAM_i	4.20	4.53	5.21	−27.38	−27.05	−26.36	0.331	1.013	0.7495	18
OMEGACAM_z	4.01	4.51	5.55	−27.56	−27.07	−26.03	0.493	1.534	0.8842	18
VIRCAM_Z	4.02	4.51	5.56	−27.56	−27.07	−26.01	0.491	1.546	0.8899	19
VIRCAM_Y	3.93	4.51	5.87	−27.64	−27.07	−25.70	0.577	1.940	1.0253	19
VIRCAM_H	3.65	4.54	6.34	−27.93	−27.03	−25.23	0.892	2.691	1.2535	19
VIRCAM_J	3.32	4.66	7.05	−28.25	−26.91	−24.53	1.335	3.721	1.6430	19
VIRCAM_Ks	3.27	5.07	8.04	−28.30	−26.50	−23.53	1.797	4.767	2.1494	19
SkyMapper_u	5.33	6.32	5.40	−26.24	−25.25	−26.17	0.989	0.073	0.3590	20
SkyMapper_v	5.81	6.09	5.31	−25.77	−25.49	−26.26	0.280	−0.493	0.3836	20
SkyMapper_g	5.03	4.94	4.78	−26.55	−26.63	−26.79	−0.082	−0.247	0.5075	20
SkyMapper_r	4.56	4.66	4.91	−27.02	−26.91	−26.66	0.104	0.352	0.6138	20
SkyMapper_i	4.14	4.52	5.28	−27.43	−27.05	−26.29	0.377	1.137	0.7768	20
SkyMapper_z	4.00	4.50	5.62	−27.57	−27.07	−25.95	0.502	1.615	0.9143	20

References: (1) Mann & von Braun (2015), (2) Cohen et al. (2003), (3) Gunn et al. (1998), (4) National Optical Astronomy Observatories (2015), (5) Tonry et al. (2012), (6) Gwyn (2012), (7) N. Kaiser (2002, private communication), (8) Hewett et al. (2006), (9) https://github.com/lsst/throughputs/tree/master/baseline, (10) Bessell & Murphy (2012), (11) Bessell & Brett (1988), (12) Goddard Space Flight Center (2012), (13) Jarrett et al. (2011), (14) Gillett et al. (1984), (15) NASA/IPAC Infrared Science Archive (2008), (15) Space Telescope Science Institute (2017a), (16) Space Telescope Science Institute (2017b), (17) Space Telescope Science Institute (2017b). (18) https://www.eso.org/sci/facilities/paranal/instruments/omegacam/tools.html, (19) https://www.eso.org/sci/facilities/paranal/instruments/vircam/inst.html, (20) Bessell et al. (2011).

Appendix
Filter Parameters

As shown by Rieke et al. (2008) and BM12, there are a number of definitions used to characterize filter properties and frequently the names associated with these definitions these are inconsistent in the literature (BM12). For convenience, the expressions used to calculate the filter parameters are presented here and the reader is referred to Appendix E of Rieke et al. (2008), the appendix of Bessell & Murphy (2012), and the review in Bohlin et al. (2014) for more detailed discussions on the determination, history, and naming of these definitions.

The following characteristic wavelengths are only dependent on the filter shape. The mean photon wavelength (Bessell & Murphy 2012), also called mean wavelength by Tokunaga & Vacca (2005) and mean or effective wavelength by Rieke et al. (2008) is defined as

$$\lambda_{\rm mean} = \frac{\int R(\lambda)\lambda d\lambda}{\int R(\lambda)d\lambda}. \tag{2}$$

The mean flux of a source within the band is defined as

$$\langle f_\lambda \rangle = \frac{\int f_\lambda R(\lambda)\lambda d\lambda}{\int R(\lambda)\lambda d\lambda}. \tag{3}$$

The nominal wavelength of Rieke et al. (2008) is called mean energy wavelength by Bessell & Murphy (2012):

$$\lambda_{n1} = \frac{\int R(\lambda)\lambda^2 d\lambda}{\int R(\lambda)\lambda d\lambda}, \tag{4}$$

while Reach et al. (2005) define the nominal wavelength as

$$\lambda_{n2} = \frac{\int R(\lambda)d\lambda}{\int \frac{R(\lambda)d\lambda}{\lambda}}, \tag{5}$$

and in both cases minimize the color correction in a given band (Reach et al. 2005; Rieke et al. 2008).

The pivot wavelength

$$\lambda_{\rm pivot} = \sqrt{\frac{\int R(\lambda)\lambda d\lambda}{\int \frac{R(\lambda)d\lambda}{\lambda}}} \tag{6}$$

is the wavelength where $\langle f_\lambda \rangle \frac{\lambda_{\rm pivot}^2}{c} = \langle f_\nu \rangle$, and $\langle f_\lambda \rangle$ or $\langle f_\nu \rangle$ are the mean flux density within the band.

The following characteristic wavelengths also take into account the flux density of the source (f_λ). As noted by BM12, there is a multiplicity of definitions for the effective wavelength, and they propose this as the standard:

$$\lambda_{\rm eff} = \frac{\int f_\lambda(\lambda)R(\lambda)\lambda^2 d\lambda}{\int R f_\lambda(\lambda)(\lambda)\lambda d\lambda}. \tag{7}$$

The wavelength where the monochromatic flux of a source is equivalent to the average flux of the source within the band is defined as the isophotal wavelength (Cohen et al. 1992; Tokunaga & Vacca 2005; Rieke et al. 2008; BM12) for *Spitzer*:

$$f(\lambda_{\rm iso}) = \langle f_\lambda \rangle. \tag{8}$$

Because this measurement can be affected by the instrumental resolution and the presence of stellar lines (Rieke et al. 2008), when calculating the isophotal wavelength one may need to smooth the spectrum prior to the calculation (Bessell & Murphy 2012), use a continuum model, or interpolate over spectral lines (Cohen et al. 1992; Rieke et al. 2008).

The bandwidth is defined as the integral of the normalized transmission (Budding 1993), and the following definition is adopted by Rieke et al. (2008) and Mann & von Braun (2015, where it is called *effective width*):

$$\mathrm{BW} = \frac{\int R(\lambda)d\lambda}{\max[R(\lambda)]}. \tag{9}$$

The average system response is

$$\mathrm{Resp} = \frac{\int R(\lambda)d\lambda}{\int d\lambda}. \tag{10}$$

For the NIRCam filters tabulated in Space Telescope Science Institute (2017b), an effective response is adopted where

$$R_{\rm eff} = \frac{\int_{\lambda\_{\rm pivot}-\mathrm{BW}/2}^{\lambda\_{\rm pivot}+\mathrm{BW}/2} R(\lambda)d\lambda}{\mathrm{BW}}. \tag{11}$$

The *vegamag* zero-point is defined as

$$zp = +2.5\,\log_{10}\left[\frac{\int f_\lambda(\lambda)R(\lambda)\lambda d\lambda}{\int R(\lambda)\lambda d\lambda}\right], \tag{12}$$

while the flux at zero magnitude is calculated using the spectrum of Vega (corrected to have zero magnitude in all bands) such that

$$f_\nu 0 = \frac{\lambda_{\rm pivot}^2}{c}\frac{\int f_\lambda(\lambda)R(\lambda)\lambda d\lambda}{\int R(\lambda)\lambda d\lambda}, \tag{13}$$

converted into Jansky, where c is the speed of light. Table 4 shows these parameters calculated for the filters used in Table 3, where the BM12 naming is used. The table columns are defined as follows: (1) the filter name, (2) the mean photon wavelength, (3) the pivot wavelength, (4) the effective wavelength, (5) the nominal wavelength using the Rieke et al. (2008) definition, (6) the nominal wavelength using the Reach et al. (2005) definition, (7) the isophotal wavelength using the Rieke et al. (2008) definition, (8) the isophotal wavelength using the BM12 column definition, (9) the wavelength range, (10) the bandwidth, (11) the FWHM, (12) the filter response, (13) the zero-point for *vegamag*, (14) the corresponding flux density in erg $\mathrm{s^{-1}\,cm^{-2}\,\AA^{-1}}$, and (15) the corresponding flux density in Jansky.

Table 4
Filter Parameters

Filter	$\lambda_{\rm mean}$ (μm)	$\lambda_{\rm pivot}$ (μm)	$\lambda_{\rm eff}$ (μm)	λ_{n1} (μm)	λ_{n2} (μm)	λ_i (μm)	λ_i(BM12) (μm)	$\lambda_{\rm range}$ (μm)	BW (μm)	FWHM (μm)	response	zp	$f_\lambda(zp)$ (erg s^{-1} cm^{-2} Å^{-1})	f_ν(mag0) (Jy)
(1)	(2)	(3)	(4)	(5)	(6)	(7)	(8)	(9)	(10)	(11)	(12)	(13)	(14)	(15)
Johnson_U	0.3618	0.3611	0.3694	0.3633	0.3603	0.3691	0.3719	0.1238	0.0581	0.0561	0.4693	20.9170	4.29723E–09	1868.72
Johnson_B	0.4410	0.4396	0.4390	0.4438	0.4382	0.3896	0.3911	0.1856	0.0992	0.1004	0.5345	20.4951	6.33795E–09	4085.60
Johnson_V	0.5524	0.5511	0.5476	0.5551	0.5499	0.5527	0.5510	0.2657	0.0871	0.0812	0.3275	21.1011	3.62701E–09	3674.73
Cousins_R	0.6612	0.6582	0.6492	0.6674	0.6553	0.6545	0.6545	0.3322	0.1669	0.1671	0.5024	21.6781	2.13191E–09	3080.98
Cousins_I	0.8047	0.8034	0.7993	0.8074	0.8020	0.8006	0.8008	0.2163	0.1482	0.1523	0.6850	22.3469	1.15139E–09	2478.76
Tycho_Bt	0.4220	0.4212	0.4234	0.4237	0.4204	0.3944	0.3938	0.1548	0.0741	0.0739	0.4790	20.4332	6.70971E–09	3970.61
Tycho_Vt	0.5352	0.5335	0.5291	0.5389	0.5317	0.5359	0.5316	0.2263	0.1134	0.1116	0.5009	21.0088	3.94906E–09	3748.93
Hipparcos_Hp	0.5596	0.5508	0.5315	0.5780	0.5421	0.5467	0.5522	0.5772	0.2405	0.2237	0.4166	21.1107	3.59516E–09	3638.04
2MASS_J	1.2411	1.2393	1.2321	1.2445	1.2376	1.2378	1.2377	0.3523	0.1628	0.2027	0.4611	23.7442	3.17931E–10	1628.84
2MASS_H	1.6513	1.6495	1.6424	1.6551	1.6476	1.6467	1.6467	0.3826	0.2510	0.2610	0.6559	24.8385	1.16041E–10	1053.12
2MASS_Ks	2.1656	2.1638	2.1558	2.1691	2.1621	2.1622	2.1625	0.4401	0.2622	0.2785	0.5951	25.8980	4.37335E–11	683.04
SDSS_u	0.3562	0.3556	0.3607	0.3572	0.3551	0.3642	0.3663	0.0983	0.0558	0.0582	0.0616	21.0632	3.75600E–09	1584.71
SDSS_g	0.4719	0.4702	0.4673	0.4751	0.4686	0.4730	0.4747	0.1963	0.1158	0.1263	0.2132	20.6442	5.52461E–09	4075.09
SDSS_r	0.6185	0.6176	0.6142	0.6204	0.6166	0.6169	0.6169	0.1723	0.1111	0.1150	0.3170	21.4800	2.55856E–09	3254.86
SDSS_i	0.7500	0.7490	0.7459	0.7519	0.7480	0.7498	0.7483	0.1844	0.1045	0.0683	0.2397	22.1124	1.42903E–09	2674.11
SDSS_z	0.8961	0.8947	0.8925	0.8992	0.8932	0.8933	0.8971	0.2781	0.1125	0.0994	0.0318	22.6604	8.62665E–10	2303.28
DES_u	0.3879	0.3859	0.3881	0.3970	0.3839	0.3774	0.3805	0.0711	0.0278	0.0256	0.0551	20.6479	5.50603E–09	2735.17
DES_g	0.4842	0.4820	0.4776	0.4890	0.4798	0.3811	0.3794	0.1663	0.1141	0.1299	0.2573	20.7091	5.20407E–09	4033.18
DES_r	0.6439	0.6423	0.6374	0.6470	0.6408	0.6379	0.6373	0.1901	0.1383	0.1484	0.3826	21.6052	2.27988E–09	3137.37
DES_i	0.7821	0.7807	0.7758	0.7848	0.7792	0.7626	0.7792	0.4647	0.1393	0.1482	0.1696	22.2523	1.25624E–09	2553.68
DES_z	0.9172	0.9158	0.9139	0.9196	0.9145	0.9574	0.9235	0.6876	0.1270	0.1479	0.1043	22.7104	8.23857E–10	2304.99
DES_Y	0.9877	0.9866	0.9830	0.9893	0.9855	0.9979	0.9898	0.1830	0.0680	0.0664	0.1642	22.9192	6.79718E–10	2207.09
PS1_g	0.4866	0.4849	0.4811	0.4900	0.4832	0.4866	0.4879	0.1707	0.1166	0.1256	0.3430	20.7241	5.13274E–09	4025.81
PS1_r	0.6215	0.6201	0.6156	0.6241	0.6188	0.6195	0.6200	0.1768	0.1318	0.1404	0.5121	21.4901	2.53499E–09	3251.66
PS1_i	0.7545	0.7535	0.7504	0.7564	0.7525	0.7525	0.7531	0.1659	0.1243	0.0698	0.6509	22.1328	1.40245E–09	2656.00
PS1_z	0.8679	0.8674	0.8669	0.8690	0.8669	0.8597	0.8662	0.1519	0.0966	0.1034	0.5596	22.5824	9.26899E–10	2326.30
PS1_Y	0.9633	0.9628	0.9614	0.9645	0.9622	0.9645	0.9621	0.1997	0.0616	0.0629	0.1893	22.8407	7.30650E–10	2259.11
cfhtls_u	0.3811	0.3803	0.3895	0.3829	0.3794	0.3810	0.3813	0.2267	0.0575	0.0654	0.1078	20.6447	5.52249E–09	2663.85
cfhtls_g	0.4862	0.4844	0.4803	0.4899	0.4826	0.4787	0.3774	0.2072	0.1322	0.1434	0.4045	20.7182	5.16084E–09	4039.99
cfhtls_r	0.6258	0.6248	0.6212	0.6279	0.6237	0.6241	0.6237	0.2001	0.1099	0.1219	0.3026	21.5171	2.47266E–09	3219.42
cfhtls_i	0.7690	0.7678	0.7638	0.7715	0.7666	0.7662	0.7667	0.2264	0.1221	0.1367	0.2594	22.1959	1.32325E–09	2602.12
cfhtls_z	0.8870	0.8859	0.8845	0.8894	0.8848	0.8840	0.8856	0.2270	0.0998	0.0936	0.1217	22.6349	8.83167E–10	2312.11
CFHT_12kx8k_B	0.4407	0.4399	0.4400	0.4424	0.4390	0.3989	0.3879	0.2573	0.0619	0.0605	0.2405	20.4681	6.49800E–09	4193.87
CFHT_12kx8k_R	0.6621	0.6610	0.6578	0.6642	0.6600	0.6591	0.6581	0.1721	0.1077	0.1181	0.6257	21.7046	2.08038E–09	3032.27
CFHT_12kx8k_I	0.8183	0.8159	0.8096	0.8231	0.8136	0.8077	0.8107	0.2585	0.1921	0.2139	0.7409	22.3816	1.11520E–09	2476.56
UKIRT_z	0.8831	0.8826	0.8823	0.8840	0.8822	0.8820	0.8812	0.1403	0.0879	0.0926	0.1194	22.6261	8.90324E–10	2313.54
UKIRT_Y	1.0319	1.0315	1.0299	1.0329	1.0310	1.0307	1.0321	0.1569	0.1008	0.1034	0.1194	23.0663	5.93591E–10	2106.53
UKIRT_J	1.2511	1.2502	1.2462	1.2529	1.2492	1.2476	1.2490	0.2386	0.1475	0.1589	0.1321	23.7842	3.06416E–10	1597.42
UKIRT_H	1.6383	1.6360	1.6271	1.6430	1.6337	1.6313	1.6324	0.4649	0.2773	0.2918	0.1586	24.8055	1.19624E–10	1067.96
UKIRT_K	2.2085	2.2060	2.1950	2.2135	2.2035	2.2017	2.2032	0.5488	0.3276	0.3413	0.1422	25.9737	4.07863E–11	662.09
LSST_u	0.3671	0.3665	0.3743	0.3681	0.3660	0.3748	0.3724	0.0906	0.0547	0.0623	0.0829	20.8555	4.54799E–09	2038.03
LSST_g	0.4827	0.4808	0.4768	0.4864	0.4789	0.4841	0.4859	0.1799	0.1333	0.1426	0.3027	20.7014	5.24138E–09	4041.31
LSST_r	0.6223	0.6210	0.6165	0.6250	0.6197	0.6206	0.6210	0.1685	0.1338	0.1343	0.3605	21.4946	2.52446E–09	3247.24
LSST_i	0.7546	0.7537	0.7506	0.7565	0.7527	0.7527	0.7533	0.1565	0.1209	0.0680	0.3490	22.1336	1.40133E–09	2655.04
LSST_z	0.8691	0.8686	0.8680	0.8702	0.8680	0.8622	0.8681	0.1350	0.0994	0.1022	0.3269	22.5857	9.24140E–10	2325.47
LSST_y	0.9710	0.9705	0.9688	0.9722	0.9699	0.9686	0.9717	0.1828	0.0814	0.0857	0.1259	22.8627	7.16026E–10	2249.34

Table 4
(Continued)

Filter (1)	$\lambda_{\rm mean}$ (μm) (2)	$\lambda_{\rm pivot}$ (μm) (3)	$\lambda_{\rm eff}$ (μm) (4)	λ_{n1} (μm) (5)	λ_{n2} (μm) (6)	λ_i (μm) (7)	λ_i(BM12) (μm) (8)	$\lambda_{\rm range}$ (μm) (9)	BW (μm) (10)	FWHM (μm) (11)	response (12)	zp (13)	$f_\lambda(zp)$ (erg s^{-1} cm^{-2} Å^{-1}) (14)	f_ν(mag0) (Jy) (15)
Bessell_Murphy_U	0.3604	0.3597	0.3674	0.3617	0.3591	0.3674	0.3680	0.1098	0.0621	0.0628	0.5656	20.9560	4.14586E–09	1789.43
Bessell_Murphy_B	0.4391	0.4378	0.4369	0.4420	0.4364	0.4601	0.3914	0.1796	0.0916	0.0894	0.5098	20.4800	6.42715E–09	4108.32
Bessell_Murphy_V	0.5501	0.5489	0.5457	0.5525	0.5477	0.5513	0.5483	0.2495	0.0875	0.0836	0.3507	21.0884	3.66982E–09	3687.87
Bessell_Murphy_R	0.6554	0.6524	0.6436	0.6616	0.6495	0.6483	0.6483	0.3393	0.1485	0.1447	0.4375	21.6485	2.19072E–09	3110.41
Bessell_Murphy_I	0.7996	0.7984	0.7943	0.8023	0.7971	0.7956	0.7960	0.1996	0.1427	0.1498	0.7147	22.3268	1.17294E–09	2493.70
Bessell_Murphy_Bt	0.4198	0.4190	0.4215	0.4214	0.4182	0.3928	0.3941	0.1447	0.0719	0.0719	0.4966	20.4308	6.72504E–09	3938.09
Bessell_Murphy_Vt	0.5315	0.5300	0.5266	0.5345	0.5285	0.5283	0.5295	0.2096	0.0993	0.0963	0.4737	20.9915	4.01224E–09	3759.32
Bessell_Murphy_Hp	0.5429	0.5349	0.5188	0.5595	0.5271	0.5694	0.5352	0.5289	0.2269	0.2117	0.4290	21.0316	3.86674E–09	3691.00
Bessell_88_J	1.2369	1.2347	1.2258	1.2412	1.2325	1.2322	1.2326	0.3593	0.2029	0.2066	0.5308	23.7318	3.21587E–10	1635.23
Bessell_88_H	1.6472	1.6450	1.6365	1.6517	1.6428	1.6406	1.6414	0.3393	0.2845	0.2984	0.8301	24.8263	1.17350E–10	1059.24
Bessell_88_K	2.1683	2.1663	2.1574	2.1721	2.1644	2.1596	2.1637	0.3593	0.2837	0.3048	0.7738	25.9019	4.35755E–11	682.12
Bessell_88_L	3.4838	3.4797	3.4602	3.4919	3.4756	3.4728	3.4733	0.7186	0.4583	0.5103	0.5611	27.8367	7.33364E–12	296.20
Bessell_88_Lprime	3.8285	3.8247	3.8063	3.8362	3.8208	3.8154	3.8182	0.6786	0.5339	0.5880	0.7632	28.2347	5.08305E–12	248.03
Bessell_88_M	4.7369	4.7347	4.7250	4.7411	4.7326	4.7241	4.7325	0.5589	0.3498	0.2044	0.3127	29.1335	2.22134E–12	166.11
GALEX_FUV	0.1539	0.1535	0.1549	0.1546	0.1532	0.1464	0.1469	0.0453	0.0255	0.0228	0.0106	20.4239	6.76768E–09	531.97
GALEX_NUV	0.2316	0.2301	0.2304	0.2345	0.2286	0.2272	0.2269	0.1185	0.0730	0.0796	0.0193	20.8469	4.58413E–09	809.45
WISE_1	3.4003	3.3897	3.3387	3.4204	3.3792	3.3687	3.3722	1.3441	0.6628	0.6358	0.4930	27.7140	8.21074E–12	314.69
WISE_2	4.6520	4.6406	4.5870	4.6746	4.6293	4.6204	4.6199	1.4623	1.0423	1.1073	0.7128	29.0322	2.43841E–12	175.16
WISE_3	12.8114	12.5705	11.3086	13.2371	12.3341	11.6601	12.0626	18.3366	5.5114	6.2771	0.3003	33.1194	5.65225E–14	29.79
WISE_4	22.3753	22.3142	22.0230	22.5013	22.2533	22.1724	22.1950	8.8919	4.1023	3.6087	0.4613	35.7525	5.00014E–15	8.30
IRAS12	11.5406	11.3562	10.4650	11.8905	11.1747	10.8564	10.9983	7.4850	5.9671	6.9307	0.7971	32.7211	8.15757E–14	35.09
IRAS25	23.8767	23.6079	22.2580	24.3900	23.3421	23.1021	23.0659	14.9700	10.0234	11.2592	0.6688	35.9191	4.28907E–15	7.97
IRAS60	61.4459	60.3699	54.5695	63.3790	59.3127	52.8094	58.0207	53.8919	30.4317	32.7622	0.5646	39.9327	1.06394E–16	1.29
IRAS100	101.9433	101.1267	96.9972	103.5466	100.3167	99.6179	99.4636	69.8599	33.2387	32.2401	0.4754	42.2860	1.21782E–17	0.42
IRAC_3.6	3.5573	3.5508	3.5204	3.5701	3.5443	3.5375	3.5400	0.8893	0.6836	0.7432	0.3639	27.9174	6.80809E–12	286.32
IRAC_4.5	4.5049	4.4960	4.4543	4.5228	4.4870	4.4785	4.4786	1.3434	0.8650	1.0097	0.3529	28.9037	2.74485E–12	185.07
IRAC_5.8	5.7386	5.7245	5.6564	5.7664	5.7104	5.6999	5.6972	1.6151	1.2562	1.3912	0.1105	29.9163	1.08012E–12	118.07
IRAC_8.0	7.9274	7.8842	7.6741	8.0118	7.8413	7.7845	7.8010	3.3582	2.5292	2.8311	0.2365	31.2516	3.15764E–13	65.47
IRS_16	16.0478	15.9222	15.4020	16.3590	15.7975	15.7463	15.7090	22.8531	4.7674	5.4763	0.6163	34.2569	1.98254E–14	16.77
IRS_22	22.6224	22.4704	21.7563	22.9355	22.3193	22.2729	22.1796	18.7995	7.0115	7.3067	0.8122	35.7499	5.01246E–15	8.44
MIPS_24	23.8436	23.7592	23.3583	24.0181	23.6750	23.6079	23.5923	12.6666	5.2969	5.3248	0.4181	36.0180	3.91555E–15	7.37
MIPS_70	72.5564	71.9861	69.3644	73.7885	71.4202	70.8090	70.9157	60.4363	21.3011	18.9838	0.3527	40.8081	4.75089E–17	0.82
MIPS_160	156.9627	156.4274	153.6888	158.0193	155.8939	155.4756	155.3366	92.3398	35.7629	34.5528	0.3872	44.2365	2.02017E–18	0.16
ACS_F330W	0.3522	0.3521	0.3523	0.3525	0.3520	0.3485	0.3593	0.0474	0.0261	0.0272	0.0454	21.2385	3.19592E–09	1321.74
ACS_F410W	0.4069	0.4064	0.4096	0.4078	0.4059	0.4535	0.3954	0.0890	0.0522	0.0543	0.2040	20.4195	6.79505E–09	3743.07
ACS_F435W	0.4338	0.4328	0.4341	0.4358	0.4318	0.3892	0.3940	0.1330	0.0863	0.0935	0.2387	20.4608	6.54181E–09	4087.92
ACS_F475W	0.4766	0.4747	0.4710	0.4802	0.4728	0.4812	0.4805	0.1781	0.1359	0.1437	0.2807	20.6676	5.40703E–09	4064.13
ACS_F555W	0.5373	0.5361	0.5333	0.5398	0.5349	0.5339	0.5329	0.1715	0.1125	0.1240	0.2408	21.0244	3.89261E–09	3731.78
ACS_F606W	0.5960	0.5922	0.5812	0.6035	0.5883	0.5895	0.5917	0.2601	0.1996	0.2323	0.3588	21.3334	2.92845E–09	3425.32
ACS_F625W	0.6325	0.6312	0.6267	0.6352	0.6298	0.6295	0.6307	0.1715	0.1308	0.1416	0.3372	21.5483	2.40256E–09	3192.67
ACS_F775W	0.7707	0.7694	0.7654	0.7732	0.7682	0.7682	0.7680	0.1874	0.1320	0.1511	0.3011	22.2032	1.31439E–09	2595.74
ACS_F814W	0.8086	0.8059	0.7987	0.8142	0.8031	0.7990	0.8000	0.2891	0.1739	0.1856	0.2654	22.3391	1.15969E–09	2512.22
ACS_F850LP	0.9030	0.9016	0.8994	0.9060	0.9001	0.9006	0.9006	0.2534	0.1247	0.1210	0.1230	22.6773	8.49320E–10	2302.73
WFC3_F218W	0.2233	0.2229	0.2233	0.2242	0.2224	0.3635	0.3786	0.0570	0.0330	0.0340	0.0239	20.8017	4.77894E–09	791.70
WFC3_F225W	0.2379	0.2372	0.2374	0.2392	0.2365	0.2350	0.2335	0.0975	0.0467	0.0470	0.0404	20.9087	4.33036E–09	812.62
WFC3_F336W	0.3359	0.3355	0.3359	0.3366	0.3351	0.3371	0.3523	0.0714	0.0512	0.0550	0.1403	21.1944	3.32855E–09	1249.55

Table 4
(Continued)

Filter (1)	λ_{mean} (μm) (2)	λ_{pivot} (μm) (3)	λ_{eff} (μm) (4)	λ_{n1} (μm) (5)	λ_{n2} (μm) (6)	λ_i (μm) (7)	λ_i(BM12) (μm) (8)	λ_{range} (μm) (9)	BW (μm) (10)	FWHM (μm) (11)	response (12)	zp (13)	$f_{\lambda}(zp)$ (erg s^{-1} cm^{-2} Å^{-1}) (14)	f_{ν}(mag0) (Jy) (15)
WFC3_F390W	0.3935	0.3924	0.4023	0.3956	0.3914	0.4522	0.3885	0.1247	0.0893	0.0948	0.1763	20.5639	5.94869E–09	3055.96
WFC3_F438W	0.4331	0.4326	0.4324	0.4340	0.4322	0.3884	0.3983	0.0849	0.0614	0.0673	0.1745	20.4103	6.85275E–09	4278.69
WFC3_F475W	0.4792	0.4774	0.4734	0.4829	0.4755	0.4763	0.4835	0.1671	0.1342	0.1481	0.2154	20.6805	5.34326E–09	4061.51
WFC3_F555W	0.5335	0.5308	0.5238	0.5389	0.5282	0.5309	0.5293	0.2846	0.1564	0.1579	0.1558	20.9843	4.03892E–09	3796.05
WFC3_F606W	0.5925	0.5887	0.5783	0.5999	0.5850	0.5917	0.5883	0.2561	0.2184	0.2298	0.2472	21.3170	2.97294E–09	3437.24
WFC3_F625W	0.6258	0.6241	0.6188	0.6291	0.6225	0.6222	0.6241	0.1762	0.1460	0.1573	0.2323	21.5086	2.49207E–09	3238.08
WFC3_F775W	0.7660	0.7648	0.7611	0.7684	0.7637	0.7642	0.7636	0.1752	0.1170	0.1455	0.1555	22.1828	1.33934E–09	2613.48
WFC3_F814W	0.8058	0.8030	0.7955	0.8117	0.8001	0.7956	0.7962	0.2746	0.1540	0.1518	0.1303	22.3259	1.17397E–09	2524.73
WFC3_F098m	0.9877	0.9864	0.9828	0.9903	0.9852	0.9872	0.9842	0.2085	0.1570	0.1694	0.3524	22.9160	6.81702E–10	2212.63
WFC3_F105W	1.0585	1.0551	1.0432	1.0652	1.0517	1.0560	1.0530	0.3290	0.2650	0.2917	0.4149	23.1459	5.51635E–10	2048.30
WFC3_F125W	1.2516	1.2486	1.2365	1.2576	1.2456	1.2455	1.2436	0.3427	0.2845	0.3005	0.4553	23.7673	3.11218E–10	1618.43
WFC3_F140W	1.3969	1.3922	1.3733	1.4061	1.3875	1.3804	1.3840	0.4438	0.3842	0.3941	0.4807	24.1788	2.13053E–10	1377.41
WFC3_F160W	1.5392	1.5370	1.5279	1.5436	1.5348	1.5322	1.5341	0.3302	0.2682	0.2874	0.4481	24.5692	1.48698E–10	1171.80
WFPC2_F218W	0.2214	0.2207	0.2205	0.2228	0.2200	0.3769	0.3781	0.0510	0.0451	0.0436	0.0026	20.7838	4.85820E–09	789.30
WFPC2_F300W	0.3013	0.2992	0.3039	0.3066	0.2972	0.2382	0.5499	0.1473	0.0857	0.0867	0.0116	21.0950	3.64742E–09	1089.44
WFPC2_F450W	0.4574	0.4556	0.4547	0.4608	0.4539	0.3830	0.3831	0.1730	0.0875	0.1078	0.0439	20.5907	5.80384E–09	4019.36
WFPC2_F555W	0.5468	0.5442	0.5373	0.5519	0.5417	0.5437	0.5416	0.2717	0.1456	0.1558	0.0604	21.0621	3.75986E–09	3714.54
WFPC2_F606W	0.6035	0.6001	0.5902	0.6101	0.5967	0.6009	0.5993	0.2677	0.1888	0.2002	0.1017	21.3763	2.81505E–09	3381.55
WFPC2_F702W	0.6945	0.6919	0.6841	0.6997	0.6893	0.6885	0.6884	0.2613	0.1666	0.1875	0.0920	21.8481	1.82293E–09	2910.78
WFPC2_F814W	0.8029	0.8002	0.7930	0.8087	0.7974	0.7930	0.7938	0.2859	0.1485	0.1455	0.0548	22.3159	1.18478E–09	2530.29
NIC2_F110W	1.1353	1.1235	1.0840	1.1575	1.1119	1.1232	1.1204	0.6564	0.4284	0.5272	0.1111	23.3646	4.50974E–10	1898.82
NIC2_F160W	1.6074	1.6030	1.5859	1.6159	1.5987	1.5932	1.5959	0.5042	0.3416	0.4013	0.1681	24.7184	1.29607E–10	1110.96
NIC3_F110W	1.1326	1.1200	1.0788	1.1561	1.1076	1.1142	1.1156	0.6568	0.4253	0.5883	0.1013	23.3547	4.55131E–10	1904.49
NIC3_F160W	1.6085	1.6042	1.5872	1.6169	1.5999	1.5965	1.5968	0.4967	0.3394	0.3987	0.1595	24.7213	1.29270E–10	1109.63
NIRCAM_F070W	0.7066	0.7046	0.6991	0.7114	0.7027	0.7053	0.7048	0.1896	0.1325	0.1600	0.1732	21.9113	1.71987E–09	2848.45
NIRCAM_F090W	0.9047	0.9025	0.8988	0.9093	0.9003	0.9039	0.9039	0.2383	0.1943	0.2101	0.2599	22.6730	8.52676E–10	2316.81
NIRCAM_F115W	1.1570	1.1543	1.1435	1.1624	1.1515	1.1526	1.1523	0.3155	0.2246	0.2683	0.2792	23.4729	4.08160E–10	1813.92
NIRCAM_F140M	1.4060	1.4053	1.4024	1.4074	1.4046	1.4064	1.4038	0.2186	0.1425	0.1478	0.2786	24.2262	2.03956E–10	1343.59
NIRCAM_F150W	1.5040	1.5007	1.4873	1.5104	1.4975	1.4974	1.4961	0.4093	0.3180	0.3371	0.3510	24.4711	1.62767E–10	1222.81
NIRCAM_F150W2	1.7039	1.6588	1.4796	1.7864	1.6150	1.6383	1.5932	1.6908	1.1753	1.3255	0.3248	24.7096	1.30667E–10	1199.33
NIRCAM_F162M	1.6281	1.6272	1.6244	1.6297	1.6264	1.6255	1.6263	0.2522	0.1683	0.1714	0.2940	24.7932	1.20984E–10	1068.60
NIRCAM_F164N	1.6446	1.6445	1.6446	1.6446	1.6445	1.6386	1.6441	0.0602	0.0200	0.0179	0.1433	24.8561	1.14173E–10	1029.98
NIRCAM_F182M	1.8466	1.8452	1.8389	1.8494	1.8437	1.8423	1.8435	0.3335	0.2377	0.2460	0.3430	25.2723	7.78176E–11	883.75
NIRCAM_F187N	1.8739	1.8739	1.8737	1.8740	1.8739	1.8698	1.8731	0.0651	0.0237	0.0211	0.1650	25.3720	7.09931E–11	831.55
NIRCAM_F200W	1.9934	1.9886	1.9681	2.0028	1.9839	1.9803	1.9828	0.5611	0.4566	0.4717	0.4016	25.5530	6.00903E–11	792.68
NIRCAM_F200W	1.9934	1.9886	1.9681	2.0028	1.9839	1.9803	1.9828	0.5611	0.4566	0.4717	0.4016	25.5530	6.00903E–11	792.68
NIRCAM_F210M	2.0964	2.0955	2.0908	2.0982	2.0945	2.0956	2.0946	0.2955	0.2065	0.2090	0.3391	25.7709	4.91626E–11	720.06
NIRCAM_F250M	2.5038	2.5032	2.5006	2.5049	2.5027	2.5046	2.5026	0.2410	0.1800	0.1826	0.2979	26.4931	2.52780E–11	528.36
NIRCAM_F277W	2.7694	2.7618	2.7280	2.7845	2.7542	2.7476	2.7471	0.8977	0.6828	0.7111	0.3129	26.8793	1.77123E–11	450.64
NIRCAM_F300M	2.9908	2.9892	2.9819	2.9941	2.9875	2.9862	2.9852	0.5259	0.3153	0.3264	0.2353	27.2152	1.29998E–11	387.46
NIRCAM_F322W2	3.2668	3.2320	3.0736	3.3335	3.1976	3.1789	3.1733	1.7937	1.3563	1.5827	0.3959	27.4646	1.03319E–11	359.99
NIRCAM_F323N	3.2370	3.2369	3.2368	3.2370	3.2369	3.2368	3.2375	0.0836	0.0385	0.0386	0.1466	27.5412	9.62799E–12	336.50
NIRCAM_F335M	3.3640	3.3621	3.3539	3.3676	3.3603	3.3592	3.3582	0.6118	0.3520	0.3608	0.2626	27.6991	8.32451E–12	313.89
NIRCAM_F356W	3.5768	3.5684	3.5287	3.5935	3.5600	3.5553	3.5532	1.0833	0.7811	0.8407	0.3766	27.9334	6.70861E–12	284.94
NIRCAM_F405N	4.0517	4.0517	4.0516	4.0517	4.0516	4.0475	4.0515	0.1108	0.0455	0.0460	0.1736	28.5039	3.96684E–12	217.21
NIRCAM_F410M	4.0844	4.0822	4.0723	4.0887	4.0801	4.0791	4.0790	0.7083	0.4379	0.4375	0.3096	28.5111	3.94060E–12	219.05

Table 4
(Continued)

Filter (1)	λ_{mean} (μm) (2)	λ_{pivot} (μm) (3)	λ_{eff} (μm) (4)	λ_{n1} (μm) (5)	λ_{n2} (μm) (6)	λ_i (μm) (7)	λ_i(BM12) (μm) (8)	λ_{range} (μm) (9)	BW (μm) (10)	FWHM (μm) (11)	response (12)	zp (13)	$f_\lambda(zp)$ (erg s^{-1} cm^{-2} Å^{-1}) (14)	f_ν(mag0) (Jy) (15)
NIRCAM_F430M	4.2818	4.2813	4.2785	4.2829	4.2807	4.2806	4.2811	0.3664	0.2277	0.2312	0.3109	28.7127	3.27266E−12	200.09
NIRCAM_F444W	4.4157	4.4040	4.3496	4.4392	4.3923	4.4440	4.3830	2.6004	1.0316	1.1055	0.2042	28.8119	2.98700E−12	193.24
NIRCAM_F460M	4.6293	4.6285	4.6229	4.6308	4.6276	4.6253	4.6192	0.4007	0.2288	0.2323	0.2433	29.0433	2.41358E−12	172.47
NIRCAM_F466N	4.6545	4.6544	4.6540	4.6545	4.6544	4.6496	4.6544	0.1311	0.0536	0.0520	0.1347	29.0995	2.29198E−12	165.62
NIRCAM_F470N	4.7078	4.7078	4.7078	4.7079	4.7078	4.7054	4.7077	0.1196	0.0510	0.0495	0.1299	29.1127	2.26424E−12	167.39
NIRCAM_F480M	4.8181	4.8167	4.8094	4.8206	4.8154	4.8314	4.8197	0.5449	0.3073	0.3145	0.2253	29.2044	2.08078E−12	161.03
MIRI_F560W	5.6462	5.6362	5.5880	5.6661	5.6262	5.6138	5.6161	1.6516	0.9980	1.1178	0.1893	29.8562	1.14167E−12	120.97
MIRI_F770W	7.6669	7.6428	7.5260	7.7145	7.6188	7.5950	7.5977	2.4617	1.9647	2.1026	0.2962	31.1385	3.50433E−13	68.28
MIRI_F1000W	9.9694	9.9544	9.8806	9.9994	9.9394	9.9255	9.9272	2.4395	1.7910	1.8730	0.2867	32.2809	1.22357E−13	40.44
MIRI_F1130W	11.3111	11.3087	11.2962	11.3161	11.3062	11.3035	11.3050	1.5212	0.7336	0.7128	0.1577	32.8409	7.30515E−14	31.16
MIRI_F1500W	15.0929	15.0651	14.9272	15.1485	15.0373	15.0153	15.0107	4.3004	2.9217	3.1126	0.2387	34.0608	2.37513E−14	17.98
MIRI_F1800W	18.0088	17.9865	17.8760	18.0536	17.9641	17.9332	17.9422	4.7688	2.9569	2.9851	0.2070	34.8322	1.16713E−14	12.59
MIRI_F2100W	20.8425	20.7950	20.5607	20.9372	20.7476	20.7067	20.6991	7.1237	4.5749	4.6813	0.1953	35.4510	6.60100E−15	9.52
MIRI_F2550W	25.4081	25.3639	25.1519	25.4992	25.3197	25.2881	25.2803	8.0027	3.6615	3.4294	0.1019	36.3163	2.97500E−15	6.38
NIRISS_F090W	0.9058	0.9031	0.8985	0.9134	0.9004	0.9071	0.9095	0.2404	0.1833	0.2093	0.5295	22.6748	8.51330E−10	2316.26
NIRISS_F115W	1.1528	1.1499	1.1388	1.1588	1.1470	1.1490	1.1491	0.3180	0.2499	0.2699	0.5486	23.4581	4.13773E−10	1824.86
NIRISS_F140M	1.4054	1.4044	1.4010	1.4075	1.4035	1.4048	1.4034	0.2236	0.1424	0.1481	0.4086	24.2231	2.04526E−10	1345.65
NIRISS_F150W	1.4970	1.4936	1.4797	1.5040	1.4902	1.4907	1.4887	0.4145	0.3160	0.3399	0.4856	24.4520	1.65658E−10	1232.74
NIRISS_F158M	1.5851	1.5825	1.5704	1.5895	1.5799	1.5766	1.5739	0.8980	0.1990	0.2011	0.1222	24.6817	1.34061E−10	1119.85
NIRISS_F200W	1.9979	1.9930	1.9714	2.0077	1.9880	1.9857	1.9865	0.5681	0.4225	0.4741	0.5126	25.5611	5.96423E−11	790.19
NIRISS_F277W	2.7737	2.7641	2.7110	2.7910	2.7545	2.7242	2.7463	2.4443	0.6915	0.7281	0.2001	26.8736	1.78060E−11	453.79
NIRISS_F356W	3.6036	3.5926	3.5326	3.6243	3.5817	3.4346	3.5737	1.1841	0.9093	0.9242	0.5690	27.9544	6.58052E−12	283.31
NIRISS_F380M	3.8258	3.8229	3.7742	3.8284	3.8199	3.3856	3.8125	0.4586	0.2050	0.2056	0.3234	28.2278	5.11523E−12	249.36
NIRISS_F430M	4.2822	4.2792	4.2303	4.2848	4.2762	4.2904	4.2710	0.3414	0.2016	0.2135	0.3908	28.6952	3.32612E−12	203.16
NIRISS_F444W	4.4400	4.4270	4.3587	4.4653	4.4139	3.9705	4.4054	1.4206	1.0923	1.1403	0.5291	28.8293	2.93953E−12	192.16
NIRISS_F480M	4.8147	4.8113	4.7529	4.8181	4.8080	4.8294	4.7985	0.5192	0.2968	0.3026	0.3206	29.1856	2.11727E−12	163.49
OMEGACAM_u	0.3594	0.3590	0.3632	0.3602	0.3585	0.3242	0.3661	0.0851	0.0461	0.0527	0.1078	21.0647	3.75085E−09	1612.09
OMEGACAM_g	0.4751	0.4735	0.4702	0.4783	0.4719	0.3788	0.4771	0.1818	0.1150	0.1317	0.3397	20.6584	5.45315E−09	4077.99
OMEGACAM_r	0.6289	0.6276	0.6233	0.6316	0.6263	0.6260	0.6264	0.1963	0.1275	0.1351	0.3237	21.5293	2.44507E−09	3212.63
OMEGACAM_i	0.7508	0.7495	0.7453	0.7535	0.7482	0.7504	0.7491	0.2451	0.1143	0.1258	0.1920	22.1133	1.42790E−09	2675.72
OMEGACAM_z	0.8847	0.8842	0.8840	0.8856	0.8837	0.8822	0.8833	0.1677	0.0606	0.0530	0.0945	22.6336	8.84201E−10	2305.75
VIRCAM_Z	0.8950	0.8899	0.8815	0.9252	0.8849	0.8903	0.8975	1.4202	0.0929	0.0973	0.0477	22.6456	8.74504E−10	2310.18
VIRCAM_Y	1.0274	1.0253	1.0204	1.0363	1.0232	1.0250	1.0287	0.3265	0.0905	0.0924	0.1933	23.0396	6.08351E−10	2133.31
VIRCAM_H	1.2549	1.2535	1.2480	1.2586	1.2520	1.2502	1.2539	0.2619	0.1624	0.1720	0.4769	23.7910	3.04518E−10	1595.92
VIRCAM_J	1.6453	1.6430	1.6339	1.6499	1.6407	1.6374	1.6373	0.4530	0.2797	0.2905	0.5340	24.8212	1.17897E−10	1061.59
VIRCAM_Ks	2.1521	2.1494	2.1349	2.1567	2.1468	2.1840	2.1417	1.3215	0.2894	0.3078	0.1869	25.8668	4.50069E−11	693.60
SkyMapper_u	0.3616	0.3590	0.3685	0.3696	0.3565	0.3475	0.3267	0.4341	0.0456	0.0431	0.1040	21.1729	3.39505E−09	1459.58
SkyMapper_v	0.3837	0.3836	0.3874	0.3841	0.3834	0.3817	0.3831	0.0649	0.0318	0.0310	0.4905	20.6070	5.71726E−09	2805.75
SkyMapper_g	0.5099	0.5075	0.5016	0.5148	0.5051	0.5088	0.5044	0.2595	0.1477	0.1570	0.5693	20.8530	4.55807E−09	3916.05
SkyMapper_r	0.6157	0.6138	0.6078	0.6195	0.6120	0.6131	0.6134	0.2395	0.1524	0.1582	0.6359	21.4523	2.62480E−09	3298.97
SkyMapper_i	0.7778	0.7768	0.7734	0.7799	0.7758	0.7757	0.7750	0.1896	0.1202	0.1400	0.6336	22.2365	1.27465E−09	2565.56
SkyMapper_z	0.9159	0.9143	0.9119	0.9191	0.9128	0.9271	0.9206	0.2445	0.1110	0.0849	0.4540	22.7153	8.20138E−10	2286.99

ORCID iDs

Christopher N. A. Willmer https://orcid.org/0000-0001-9262-9997

References

Aumann, H. H., Beichman, C. A., Gillett, F. C., et al. 1984, ApJL, 278, L23
Beers, T. C., Flynn, K., & Gebhardt, K. 1990, AJ, 100, 32
Bessell, M., Bloxham, G., Schmidt, B., et al. 2011, PASP, 123, 789
Bessell, M., & Murphy, S. 2012, PASP, 124, 140, (BM12)
Bessell, M. S., & Brett, J. M. 1988, PASP, 100, 1134
Bessell, M. S., Castelli, F., & Plez, B. 1998, A&A, 333, 231
Binney, J., & Merrifield, M. 1998, Galactic Astronomy (Princeton, NJ: Princeton Univ. Press), 53
Blanton, M. R., Hogg, D. W., Bahcall, N. A., et al. 2003, ApJ, 592, 819
Bohlin, R. C. 2014, AJ, 147, 127
Bohlin, R. C., Gordon, K. D., & Tremblay, P.-E. 2014, PASP, 126, 711
Bohlin, R. C., Mészáros, S., Fleming, S. W., et al. 2017, AJ, 153, 234
Budding, E. 1993, Introduction to Astronomical Photometry (Cambridge: Cambridge Univ. Press), 286
Carter, B. S. 1990, MNRAS, 242, 1
Casagrande, L., Ramírez, I., Meléndez, J., & Asplund, M. 2012, ApJ, 761, 16
Cohen, M., Walker, R. G., Barlow, M. J., & Deacon, J. R. 1992, AJ, 104, 1650
Cohen, M., Wheaton, W. A., & Megeath, S. T. 2003, AJ, 126, 1090
Cousins, A. W. J. 1976, MmRAS, 81, 25
Dudok de Wit, T., Kopp, G., Fröhlich, C., & Schöll, M. 2017, GeoRL, 44, 1196
Engelke, C. W. 1992, AJ, 104, 1248
Engelke, C. W., Price, S. D., & Kraemer, K. E. 2010, AJ, 140, 1919
Falcón-Barroso, J., Sánchez-Blázquez, P., Vazdekis, A., et al. 2011, A&A, 532, A95
Fontenla, J. M., Harder, J., Livingston, W., Snow, M., & Woods, T. 2011, JGRD, 116, D20108
Fukugita, M., Shimasaku, K., & Ichikawa, T. 1995, PASP, 107, 945
Gillett, F. C., Clegg, P., Rosing, D., et al. 1984, IRAS Explanatory Supplement (Pasadena, CA: IPAC), http://irsa.ipac.caltech.edu/IRASdocs/exp.sup/toc.html
Glasse, A. & MIRI European Consortium 2015, MIRI-TN-00072-ATC issue 3
Goddard Space Flight Center 2012, Galaxy Evolution Explorer (Greenbelt, MD: GSFC), https://universe.gsfc.nasa.gov/archive/galex/
Gunn, J. E., Carr, M., Rockosi, C., et al. 1998, AJ, 116, 3040
Gwyn, S. D. J. 2012, AJ, 143, 38
Haberreiter, M., Schöll, M., Dudok de Wit, T., et al. 2017, JGRA, 122, 5910
Hewett, P. C., Warren, S. J., Leggett, S. K., & Hodgkin, S. T. 2006, MNRAS, 367, 454
Høg, E., Fabricius, C., Makarov, V. V., et al. 2000, A&A, 355, L27
Jarrett, T. H., Cohen, M., Masci, F., et al. 2011, ApJ, 735, 112
Johnson, H. L. 1955, AnAp, 18, 292
Johnson, H. L. 1966, ARA&A, 4, 193
Johnson, H. L., & Morgan, W. W. 1953, ApJ, 117, 313
Kurucz, R. L. 2005, http://kurucz.harvard.edu
Kurucz, R. L. 2011, http://kurucz.harvard.edu/stars/Sun/fsunallp.500resam501
Maíz Apellániz, J. 2006, AJ, 131, 1184
Mann, A. W., & von Braun, K. 2015, PASP, 127, 102
NASA/IPAC Infrared Science Archive 2008, Spitzer Documentation & Tools (Pasadena, CA: IRSA), http://irsa.ipac.caltech.edu/data/SPITZER/docs/spitzermission/
National Optical Astronomy Observatories 2015, The NOAO Data Handbook (Tucson, AZ: NOAO), http://ast.noao.edu/data/docs
Oke, J. B., & Gunn, J. E. 1983, ApJ, 266, 713
Peterson, D. M., Hummel, C. A., Pauls, T. A., et al. 2006, Natur, 440, 896
Prša, A., Harmanec, P., Torres, G., et al. 2016, AJ, 152, 41
Ramírez, I., Michel, R., Sefako, R., et al. 2012, ApJ, 752, 5
Reach, W. T., Megeath, S. T., Cohen, M., et al. 2005, PASP, 117, 978
Rieke, G. H., Blaylock, M., Decin, L., et al. 2008, AJ, 135, 2245
Space Telescope Science Institute 1998, SYNPHOT Users Guide (Baltimore, MD: STScI), http://stsdas.stsci.edu/Files/SynphotManual.pdf
Space Telescope Science Institute 2017a, CALSPEC Calibration Database (Baltimore, MD: STScI), http://www.stsci.edu/hst/observatory/cdbs/calspec.html
Space Telescope Science Institute 2017b, JWST Observatory and Instrumentation Documentation (Baltimore, MD: STScI), https://jwstdocs.stsci.edu/display/JTI/
Su, K. Y. L., Rieke, G. H., Malhotra, R., et al. 2013, ApJ, 763, 118
Thuillier, G., Floyd, L., Woods, T. N., et al. 2004, AdSpR, 34, 256
Thuillier, G., Hersé, M., Labs, D., et al. 2003, SoPh, 214, 1
Tokunaga, A. T., & Vacca, W. D. 2005, PASP, 117, 421
Tonry, J. L., Stubbs, C. W., Lykke, K. R., et al. 2012, ApJ, 750, 99
Woods, T. N., Chamberlin, P. C., Harder, J. W., et al. 2009, GeoRL, 36, L01101